Bulletin of the Seismological Society of America, 91, 5, pp. 1144–1157, October 2001

Finite-Source Modeling of the 1999 Taiwan (Chi-Chi) Earthquake Derived from a Dense Strong-Motion Network

by Wu-Cheng Chi, Douglas Dreger, and Anastasia Kaverina

Abstract The 1999 *Chi-Chi* earthquake (M_W 7.6) (20 September 1999, 17:47:15.9 UTC) (located at 23.853° N, 120.816° E, and depth of 7.5 km) inflicted severe regional scale damage to Taiwan. The strong-motion wavefield was captured by a dense network of stations (with average station spacing of 5 km), which represents the most complete strong-motion dataset to date to use to study the kinematic source process of an earthquake. We inverted velocity waveforms recorded by 21 stations for the spatial variation in slip on a planar fault model composed of 416 subfaults, each with a dimension of 3.5 km by 3.5 km. The planar model has a strike of N5° E and a dip of 30° E, and the inversion solves for the direction and magnitude of the slip. To account for possible temporal source complexity we allowed each subfault to slip within 10 overlapping time windows, each with a duration of 3 sec. The results show that the source is composed primarily of three major asperities, the first of which is mainly dip slip, extending from the hypocenter to the northern end of the surface rupture. In this asperity, slip occurred in two pulses separated in time by 5 sec. The dislocation rise time for each pulse is short (3–4 sec), yielding an approximate average slip velocity of 80 cm/sec. The second asperity is located at shallow depth near the northern end of the rupture where very large ground velocities were observed. This asperity is on average oblique and shows a temporal rake rotation from pure dip-slip to strike-slip. The rotating rake suggests a low initial shear-stress on the northern end of the fault. Slip in this asperity is dominated by a large pulse with a dislocation rise time of 8 sec. A station near the northern end of the surface rupture recorded a peak velocity of 390 cm/sec, which we find to be due to the constructive interference of energy radiated from the first two asperities. The third asperity is located south of the epicenter. The total moment from the three asperities is 4.1×10^{27} dyne cm, which was released over a period of 30–35 sec within an area of 900 km^2. Synthetics calculated from the three-asperity model explain 85% of the data and represent 98% of the total variance reduction. Our results indicate that slip is confined to the shallow region of the fault, deep slip patches are less constrained, and that the slip distribution may be representative of fault segmentation along the Chelungpu fault system.

Introduction

The 1999 Chi-Chi earthquake (M_W = 7.6) (20 September 1999, 17:47:15.9 UTC) (located at 23.853° N, 120.816° E, and depth of 7.5 km) inflicted severe regional damage to the island of Taiwan. It also generated the most complete near-source strong-motion dataset available with an average station spacing of 5 km. Combined with the considerable volume of geological and geophysical data collected in this region over the past decades, this event provides an excellent opportunity to study the rupture process of a large earthquake and its relation to regional tectonics.

The Chi-Chi earthquake has a predominantly thrust focal mechanism (Fig. 1; strike = 5°, dip = 34°, and rake = 65°) derived from the first motions of the strong-motion records (Chang *et al.,* 2000). Teleseismic solutions (strike = 37°, dip = 25° and rake = 96°). (Harvard Central moment tension [CMT]) and (strike = 26° dip = 27° and rake = 82°) (Yagi and Kikuchi, 1999) compare well but show some variation, which may be due to coseismic rake rotation or a nonplanar fault surface. Surface slip measurements indicate variation in rake along an 80-km N–S–trending surface rupture along Chelungpu Fault (Central Geological Survey [CGS] 2000). The surface rupture was mapped from Chusan

(Bamboo mountain) to the vicinity of Shanyi (Fig. 1a) where it bends east and develops a complex en echelon pattern. Field observations also show that the greatest surface offset (>8 m vertically) occurred near the northern end of the fault (CGS, 1999). Coincidentally, Shanyi (Fig. 1a) is also the end of a previously identified seismic belt that extends 40 km SE to Puli (Rau and Wu, 1998, Wu and Rau, 1998; Lin, 2000).

The strong-motion data recorded by the Taiwan Strong Motion Instrumentation Program (TSMIP) of the Central Weather Bureau (CWB) (Lee *et al.,* 1999) shows evidence of strong northward directivity judged by the larger horizontal peak ground velocity (HPGV) to the north than to the south (Fig. 1b). This effect is also evident in the horizontal peak ground acceleration (HPGA) on the footwall. In addition, footwall stations close to the surface break have HPGA values less than 300 cm/sec^2, while the hanging-wall stations have HPGA values greater than 500 cm/sec^2. This pattern is seen to extend 60 km north of the northernmost surface rupture. The hanging-wall amplification is less pronounced in HPGV, indicating it is frequency dependent because the integration to velocity from acceleration enhances lower frequency components. The highest HPGA (1100 cm/sec^2) is located close to the epicenter in the hanging wall on the southern segment. However, the HPGV increased northward on the hanging wall until it reached the highest value (390 cm/sec) at the northern end of the surface rupture where there is greater than 8-m vertical offset. The spatial separation between HPGA and HPGV suggests that there are differences in the rupture dynamics of the northern and southern ends of the fault, where in the north energy was radiated at relatively lower frequency compared to the south. The damage in this region is mainly due to the surface rupture and strong ground motion (Chiu and Huang, 2000). The HPGA and HPGV also indicate that there might be strong 3D path effects, which would be anticipated from the tomographic results of Cheng (2000). In fact, stations situated in sedimentary basins do show larger amplitudes and greater waveform complexity.

Yagi and Kikuchi's (1999) preliminary teleseismic inversion, reported on their website, showed a northward rupture propagation. Ma *et al.* (2000) inverted the strong-motion, teleseismic, and GPS data and found the rupture was complex with variable slip direction and rupture velocity, and these results are consistent with the results of Mori *et al.* (2000), which used teleseismic data, and with those presented in this study. Yagi and Kikuchi (2000) inverted strong-motion, teleseismic, and GPS data and found a heterogeneous slip rate. They also identified three asperities on the fault: one 10 km west of the epicenter, one 20 km north, and one about 40 km northwest and updip where large surface offsets were observed. Preliminary studies indicate a complex spatial and temporal source process with relative low rupture velocity (<2.5 km/sec) and long dislocation rise time (Chi *et al.,* 2000; Ma *et al.,* 2000; Mori *et al.,* 2000; Wu *et al.,* 2000; Yagi and Kikuchi, 2000). In order to better understand the earthquake rupture process, we have derived a finite source model using the strong-motion dataset provided by CWB of Taiwan (Lee *et al.,* 1999). The methodology used is similar to that of Hartzell and Heaton (1983), and that used in recent studies of the Hector Mine earthquake in Southern California (Dreger and Kaverina, 2000; Kaverina *et al.,* 2000). The objective of this study is to determine the slip distribution, the fault geometry, and the kinematics of the rupture process and to assess the resolution of the source parameters. We have conducted detailed sensitivity tests on station distribution, fault plane dimension, varying rake, rupture velocity, and also studied the contribution to the waveforms from each of the major asperities in our preferred model.

Finite-Source Methodology

We used strong-motion data to invert the representation theorem (equation 1) for finite source parameters (e.g., Hartzell and Heaton, 1983). The observed seismogram is related to the spatiotemporal integration of slip distributed on a plane, where,

$$U_n(\mathbf{x},t) = \int d\tau \iint \left[\left[\mu \; \hat{n}_i \; u_j \; (\xi,\tau) \right] \cdot G_{ni,j}(\mathbf{x},\xi;t-\tau) \right] d\Sigma(\xi), \quad (1)$$

where U_n is the nth component of observed velocity, μ is the rigidity, $\hat{n}_i$ is the fault orientation unit vector, u_j is the fault slip, $G_{ni,j}$ is velocity Green's function, $\mathbf{x}$ is a vector describing the relative location of the source and receiver, ξ, τ are spatial and temporal variables of integration, and $d\Sigma(\xi)$ is the area differential; Σ is a function of the spatial variable ξ.

The subscript letter n refers to the ground-motion component, and i and j are orientation indices. The quantity $\mu\hat{\mathbf{n}}_i$ u_j $(\mathbf{x},t)$ is equivalent to $m(\mathbf{x},t)$, which describes the spatial and temporal seismic moment tensor. $U_j(\boldsymbol{\xi},\tau)$ is the spatiotemporal slip information to be determined by inverting the data.

We use a linear least-squares inversion of observed velocity seismograms to compute the spatiotemporal slip distribution. Several constraining equations are also applied to improve the stability of the inversion. First, the slip is required to be everywhere positive. Second, a Laplacian smoothing operator is applied to minimize the fluctuation of slip in adjacent subfaults. The weight of the Laplacian operator is a free parameter, and we examine a range of values before settling on a weight that succeeds in providing a suitably smooth model that also results in a good level of fit to the waveform data and scalar moment derived from long period data. Third, we use surface slip constraints, which are implemented by first projecting the measured surface offsets (CGS, 2000) onto the modeled fault plane. The difference between the projected observed slip and slip on the corre-

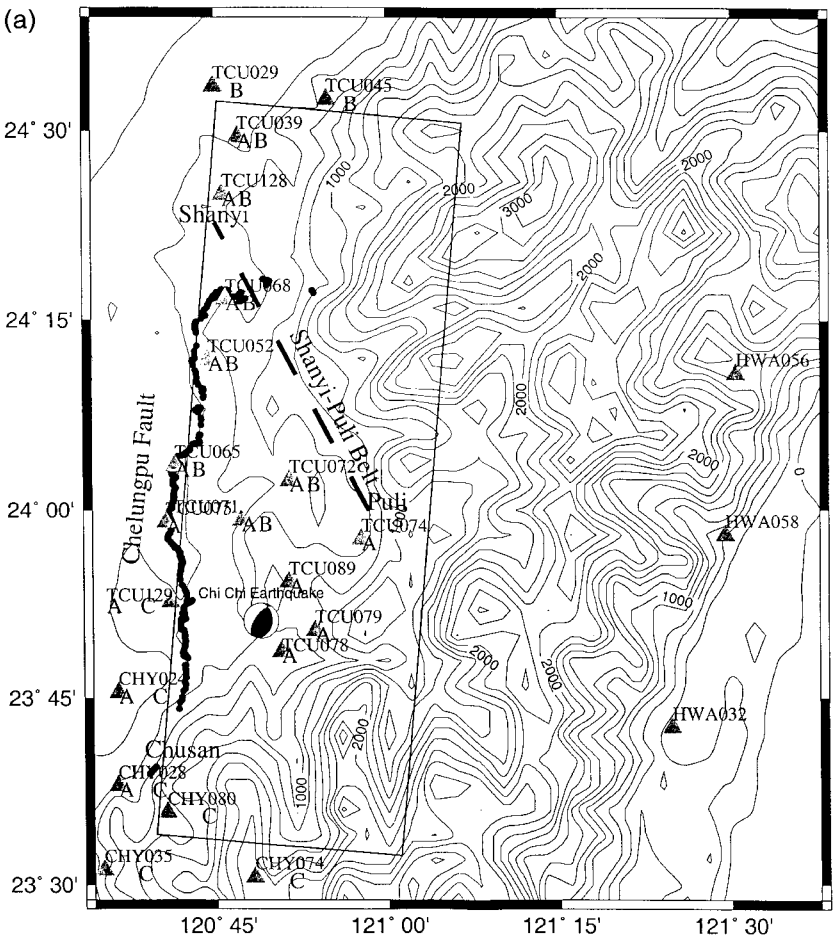

Figure 1. (a) Topographic and location map. For the location of this figure, see the rectangular box in (b). The focal mechanism of Kao and Chen (2000) is predominantly thrust. The dots show the surface rupture mapped by the CGS (1999) that extends from Chusan to the vicinity of Shanyi where the surface rupture then bends eastward and forms an en enchelon pattern. Some surface fissures were found at Puli. The locations of 21 (7 on the footwall and 14 on the hanging wall) stations used in our final inversion are shown as triangles. The letters A, B, and C below the station names identify the asperities that contributed to the seismogram at that station (see section on Preferred Model and Sensitivity Analysis for details). There is a topographic low region bounded by the towns Shanyi, Puli, and Chusan. It is in this region we find that most of the slip was confined. (b, facing page) The circles display the spatial distributions of HPGA and HPGV. The sizes of the circles are scaled according to the corresponding HPGA/HPGV values. The highest HPGA value was recorded near the epicenter in the southern part of the surface rupture. There is a notable 200 cm/sec^2 increase in average HPGA at stations located close to the fault on the hanging block. The highest HPGV was located near the northern end of the surface rupture. The HPGV pattern clearly shows the effects of northward directivity. Examples of stations where lateral heterogeneity has a strong affect are shown by arrows.

sponding subfaults is minimized. The surface slip constraint controls the distribution of slip in the shallowest row of the finite fault model and has negligible impact on the deeper subfaults.

For each subfault we simultaneously invert for pure reverse dip slip and left-lateral strike slip. The vector sum of the two components then gives the total subfault slip and the slip direction. Following the approach of Hartzell and Heaton (1983) we use a multitime window method to account for temporal heterogeneity in fault slip. This parameterization allows us to first assume a constant rupture velocity and a circular rupture front, as well as a constant dislocation rise time for a given time window. However, by allowing each subfault to rupture in subsequent time windows we allow the overall rupture velocity and rise time to vary spatially. For example, slip that occurs only in later time windows is interpreted as having a lower rupture velocity, while slip that occurs in several consecutive time windows is interpreted as having a longer rise time. Each of the individual time functions are normalized to unit area so that they integrate to total slip for the given time window. We use a minimum time function of 3 sec, which is defined as an isosceles triangle, and each subsequent window is delayed by one-half the duration (1.5 sec). The summation of the integrated time function then results in the total slip for a given subfault, and the time window duration effectively defines the maximum corner frequency and controls the ability to model higher frequencies in the data.

Station Selection and Green's Function Computation

We used the strong-motion data from the instrument-response-corrected ASCII files disseminated on CDROM by Lee *et al.* (1999). The acceleration data were integrated to velocity and filtered between 0.02 and 0.5 Hz before being resampled at 10 samples per sec. A total record span of 50 sec is used. Because there might be timing problems at some stations (Lee *et al.,* 1999), we have done several tests to avoid stations with apparent timing errors. First we aligned the acceleration seismograms to check the arrival-time moveout (Fig. 2). There was only one obvious timing error among the 30 stations that we initially considered for the inversion, and this station was removed from consideration. In Figure 2 we compare the first *P*-arrival time calculated from the 1D velocity model that we use to compute Green's functions (Table 1) with a record section of vertical-component acceleration waveforms. Overall the mean deviation between the observed and predicted arrival times is -0.1

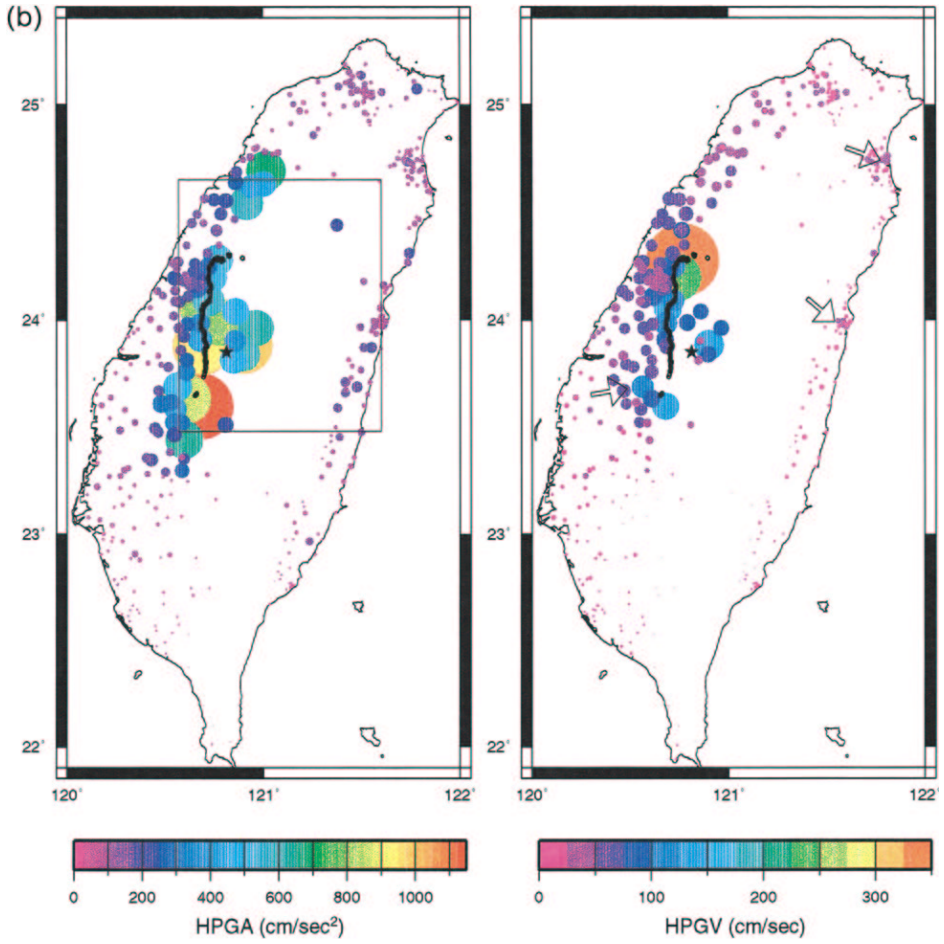

sec, with a standard deviation of 1.4 sec. In all cases the deviation is less than the duration of one time window (3 sec) and therefore has minimal impact on the inversion results. The source of the arrival time scatter could be due to clock errors, lateral heterogeneity, and difficulty in observing the initial onset due to the emergent nature of the *P* waveforms. In addition, Huang (2000) produced an animation of the observed wavefield across the network. In that study, time shifts were applied to some of the original data to make the wave propagation spatially coherent and self-consistent. We compared our unfiltered acceleration data with figure 2 of Huang (2000) and found the timing differences are generally less than 1 sec. We also compared our data with the animation, and even though these data are filtered to periods between 10 and 20 sec, we found reasonably good agreement. Based on the aforementioned results, we feel justified using the absolute timing for the 21 stations and are confident that the 1D velocity model used to compute Green's functions is a good approximation to the average crustal structure.

We further culled the dataset to maximize azimuthal coverage without overweighing a particular azimuth (Fig. 1a), and to remove stations, which appeared to be more strongly influenced by 3D heterogeneity. We examined particle motion plots for the entire dataset and compared them spatially with a recently available 3D tomographic model (Cheng, 2000). Several basin stations show large amplitudes and complex waveforms compared to adjacent hard-rock stations. These basin stations were removed and replaced with a hard-rock station if possible.

A frequency-wavenumber methodology written by Chandan Saikia (Saikia, 1994) was used to calculate a set of Green's functions based on the 1D velocity model provided in Table 1 and published in a recent 3D tomographic study by Rau and Wu (1995). This 1D model has been well tested by routine regional moment tensor studies of local and regional events (cf. Kao and Chen, 2000), and is shown in Figure 2 to agree well with the first arrival times of the data used in this study. Because of the large dimension of the fault model and the regional station coverage, Green's functions were calculated for a source-receiver range of 2 to 200 km with an increment of 3 km, and for a source depth range of 2 to 17 km with an increment of 3 km. The calculated Green's functions were filtered in the same manner as the data. Several stations are located close to the fault trace, less than the 2-km-minimum Green's function distance. We note that the center point of the shallowest 3.5 $\times$ 3.5 km subfault is at a depth of 0.9 km and 1.5 km laterally from the surface

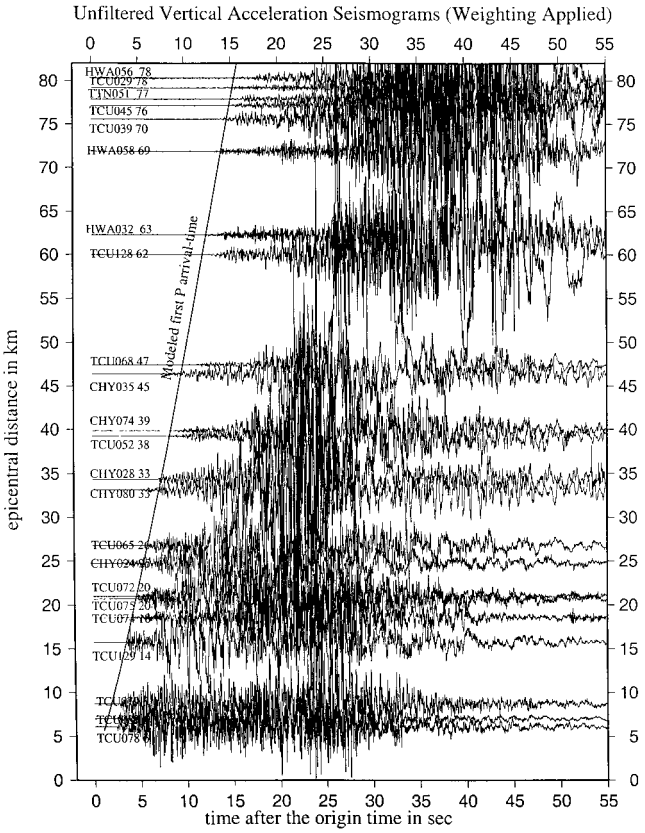

Figure 2. A common-shot-gather plot was used to check for possible timing errors of the 21 stations we used for the finite source inversion. These waveforms are unfiltered vertical acceleration data. Each trace is scaled to emphasize the beginning of the record. The first *P*-wave arrival-time curve is derived from the velocity model we used to calculate Green's functions. The mean difference between the observed first arrivals and the travel-time curve is -0.1 ± 1.4 sec demonstrating that these stations do not have any serious timing errors.

Table 1
1D Velocity Model Used for Green's Function Calculation

Thickness (km)	Depth (km)	V_p (km/sec)	V_s (km/sec)	Density (g/cm^3)	Q_p	Q_s
2.2	2.2	4.5	2.6	1.8	200	100
2.2	4.4	4.85	2.8	2.05	600	300
2.2	6.6	5.3	3.06	2.25	600	300
2.2	8.8	5.6	3.23	2.39	600	300
4.5	13.3	5.84	3.37	2.5	600	300
4.5	17.8	6.13	3.54	2.64	600	300
7.5	25.3	6.28	3.63	2.7	600	300
8.5	33.8	6.6	3.81	2.85	600	300
5	38.3	6.87	3.97	2.97	600	300
21.5	60.3	7.43	4.29	3.3	600	300
25	85.3	7.8	4.5	3.3	600	300

rupture. Because the surface slip constraint controls slip in the shallowest row of subfaults, the range of Green's function distances and depths is appropriate for the small-distance shallow-depth subfault-station pairs.

Preferred Model and Sensitivity Analysis

The location of the surface rupture and its offsets used in our fault plane parameterization were based on the field investigation by the CGS (1999). Surface evidence indicates that the fault geometry of the mainshock was complex. However, to begin the source modeling we considered a single 112 by 45.5 km single fault plane with a strike of N5°E to separate the hanging-wall stations from the footwall stations. The dip is 30°E, based on a combined regional broadband network (BATS)/teleseismic study by Kao and Chen (2000). The fault plane is composed of 416 subfaults, each with a dimension of 3.5 by 3.5 km. Each subfault was permitted to rupture in any of 10 3-sec isosceles-triangle time windows, each separated by a 1.5-sec delay. However, we also examined simpler time models, which will be discussed shortly. For each time window both pure dip slip and pure strike slip are solved for. Ten time windows on 416 subfaults each with dip-slip and strike-slip components translates to 8320 unknowns. Forty-one 50-sec seismograms from 21 stations sampled at 10 samples per sec were used in the inversion, which translates to 20,500 data points. The data are most certainly correlated, thus the actual number of data is less. The surface slip data, smoothing, and slip positivity constraining equations provide stability in the inversion.

We performed more than 80 inversions to reach our preferred model (Fig. 3), which is presented here to define its principle features. As Figure 3 shows, there are five regions of the slip model designated by the letters A–E. These regions represent areas of moment release that appear to be distinct and are herein referred to as asperities A–E. A detailed discussion of these features and the interpretation is provided in the later section (Interpretation of Preferred Model). Before discussing the interpretation, it is instructive, however, to examine the sensitivity of the finite fault slip inversion to factors such as station selection, station geometry, style of slip, rupture velocity, and rise-time heterogeneity to determine which of these features are robust.

Station Sensitivity

To examine the possibility of unmodeled 3D propagation effects at some stations and because of the possibility of unknown timing errors in the data (Lee *et al.,* 1999), we conducted a Jackknife test to investigate the sensitivity of the inversion to each station. Our initial choice of stations was governed by a desire to maximize azimuthal coverage and was predicated on the data being consistent with Huang (2000) and the first-arrival travel-time moveout as described previously. The sensitivity of groups of stations, such as those located on the hanging block, the footblock, and the northern end of the surface rupture was studied. In addition,

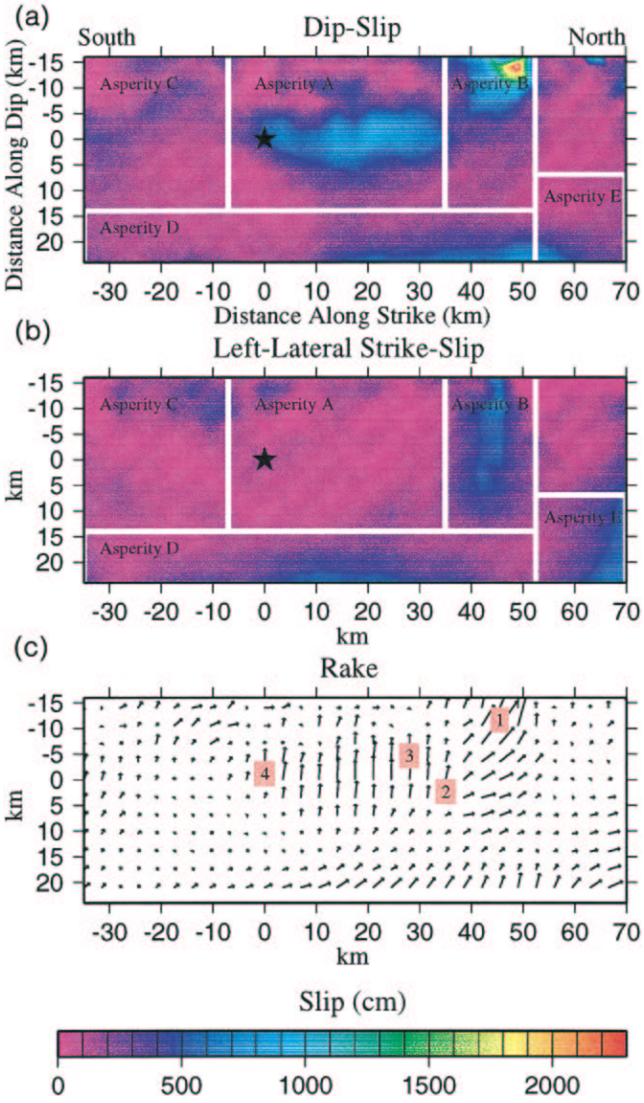

Figure 3. Best inverted slip model. A star denotes the hypocenter. There are five major asperities: asperity A is mainly dip slip within the triangular zone bounded by the towns of Shanyi, Puli, and Chusan; asperity B is oblique slip along the Shanyi-Puli belt; asperity C trends NW–SE with oblique slip. Asperity D is dip slip near Puli; and asperity E is strike slip near the NE corner. Based on our analysis, the slip pattern from asperities A, B, C are well constrained, but asperities D and E are inconclusive. Our preferred model only consists of asperities A, B, and C. (a) Dip-slip component, (b) strike-slip component, (c) vector plot showing the magnitude of total slip and the slip direction. Four locations where the dislocation rise time is investigated are labeled.

the sensitivity of the inversion to rupture velocity, time heterogeneity, and slip direction was explored.

As previously discussed there is a pronounced footwall/hanging-wall effect in the observed HPGA (Fig. 1b), and we tested inversions using only stations located on either the footwall or hanging-wall blocks. Having poor azimuthal coverage, the footwall station inversion results in extensive, excessive slip (averaging 6.1 m over the entire fault plane). The scalar moment is 1.75×10^{28} dyne cm, and the variance reduction (VR) [VR = 1 − (Σ(synthetics-data)^2/Σ(data)^2)] is 92%. The inversion using only the hanging-block stations results in the same level of fit (VR = 92%) although more stations were used. The average slip is 4.1 m, and the distribution is more coherent forming asperities similar to the preferred results (Fig. 3), which uses 21 stations (Fig. 1A). The scalar moment was found to be 7.46×10^{27} dyne cm for this inversion. Figure 1b indicates that for HPGV the hanging-wall amplification is not as strong and that it is not a factor in the inversion results. In fact, the derived scalar moment from the hanging-wall stations is less than for the footwall stations. Thus it seems that the most important consideration is the completeness of the coverage. The hanging-wall stations have greater azimuthal coverage and therefore provide greater constraint on the distribution of slip.

At the northern end of the surface rupture the largest HPGV and surface displacements were observed. Station TCU068 recorded a HPGV of 390 cm/sec and is sited on the hanging wall close to the location of the maximum surface offset (8 m vertically). When this station is omitted from the inversion the slip model is largely unchanged; however, the level of slip in asperity B is reduced by half. Other nearby stations such as TCU029, 045, 052, 128, 065, 072, and 071 were also found to constrain asperity B (Fig. 1a, 3).

The stations that control slip in the middle of the fault include TCU052, 065, 068, 071, 072, 075, 074, 079, 089, 078, and 128 (Fig. 1a). Most of these are located on the hanging block above the rupture plane. These stations were found to have two important effects. First, they resolve heterogeneity within asperity A (Fig. 3), and second, they suppress slip on the deeper portions of the model (e.g., asperities D and E). Additionally, stations HWA056, 058, and 032 are located on the hanging block to the east of the rupture plane (Fig. 1). These stations were found to provide important constraint of the deeper slip where the net effect was to suppress slip in asperities D and E.

At the southern end of the surface rupture and the fault model, stations CHY024, 028, 035, 074, and 080 require slip to be located to the south of the epicenter (asperity C in Fig. 3). These stations also seem to have moderate sensitivity to asperity A and almost no sensitivity to asperity B. Some slip south of the epicenter is consistent with the results of Yagi and Kikuchi (1999).

In summary, the 21 stations that we used maximize azimuthal and footwall/hanging-wall coverage of the rupture plane. These stations have been verified to be consistent with the *P*-wave travel time from the 1D velocity model we have assumed for the Green's functions and do not appear to suffer from significant timing errors. This subset of stations resulted from the analysis of 30 stations, where stations exhibiting either significant timing errors or possible influence from 3D structure were replaced by another nearby station.

Slip Direction Sensitivity

Surface offsets and GPS data indicate that the slip in the earthquake was predominantly dip slip, however, these data together with slightly oblique long-period thrust focal mechanisms suggest a significant strike-slip component. The finite source inverse method recovers variable slip direction by simultaneously solving for the reverse dip-slip and strike-slip (in this case left lateral) components. The vector sum of the two components gives the slip magnitude and direction. We first tested an inversion where slip was allowed to only be pure thrust. This calculation had the full 10 time window parameterization, and the results are shown in Figure 4a. For this inversion a VR of 80% was obtained, which is less than the 87% result obtained for the preferred model (Fig. 3). This inversion recovered the slip in asperities A and B. Another inversion was performed, which allowed only left-lateral strike-slip. This inversion resulted in a VR of 60% and recovered large slip at the base of the fault model. To examine the significance of the variable slip direction in the preferred model, we used the *F* test. Three *F*-ratios of the variances of the simplified models to the preferred model were computed. The variances of the simplified models were normalized by 20,500 (data points) −4160 (model parameters) = 16,340 degrees of freedom, and the variance of the preferred model was normalized by 12,180 degrees of freedom (representing twice the model parameters). The *F* statistics of the preferred model to the pure dip-slip and strike-slip models are 1.52 and 3.06, respectively, and both exceed the critical *F*-value of 1.04 representing statistical significance greater than the 99th percentile assuming uncorrelated data. The data are certainly correlated, however, and the actual significance level is less. Nevertheless our detailed analysis of the velocity seismograms presented later and other independent data sets indicate that oblique slip is required.

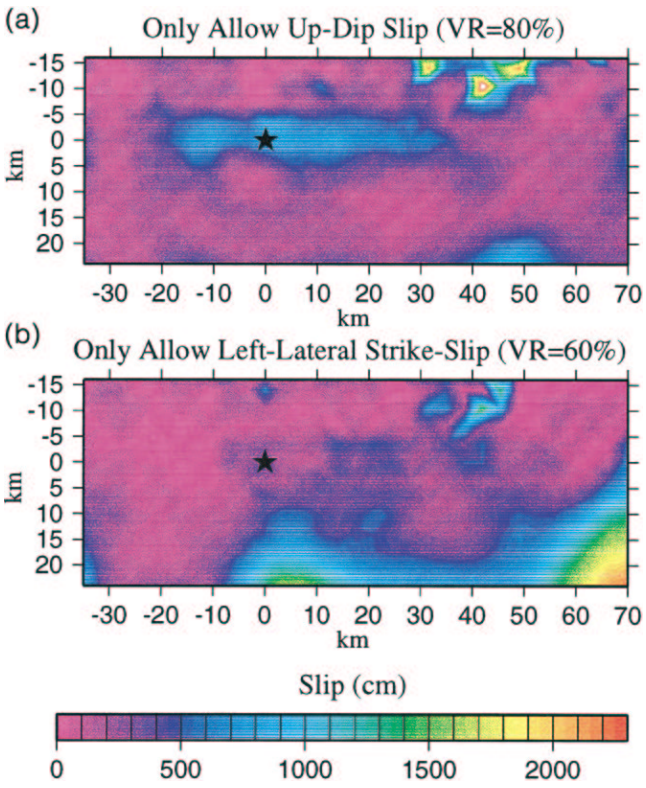

Figure 4. Rake sensitivity tests. For the inversion that only allowed updip slip we obtain a good fit and a variance reduction (VR) of 80%, compared with 87% for our best model. For this case, slip was resolved only in asperities A and B. For the inversion that only allowed left-lateral strike-slip we obtain a VR of 60% and slip is largely at the bottom of the fault plane.

Rupture Velocity Sensitivity

Rupture velocity sensitivity for the 10 time window parameterization was investigated (Fig. 5), and we found that a value of 2.6 km/sec gave the largest variance reduction, although there is a wide range (2–2.9 km/sec) that also gave good results. Values of rupture velocity less than or greater than the optimal value tend to rearrange slip in time, where slower rupture velocities produce large slip in the early time windows and faster values tend to map slip to later times. Generally we find that the data requires a substantial time delay in the occurrence of major slip. Asperities A, B, C, and D are observed in all runs where the rupture velocity is altered, although there is some variation in the distribution of slip between the asperities.

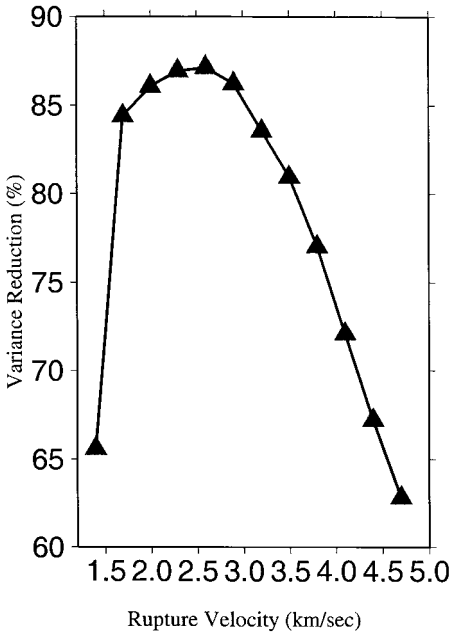

Figure 5. Rupture velocity sensitivity. Rupture velocity is tested from 1.7 km/sec to 3.2 km/sec. Our preferred model has a rupture velocity of 2.6 km/sec.

Dislocation Rise-Time Sensitivity

Our preferred model has 10 time windows to account for rupture velocity and dislocation rise-time variation. To establish a baseline we performed an inversion with only one time window. We used one 3-sec window that ruptures upon the arrival of a circular rupture front propagating at 2.6 km/sec, and obtained a variance reduction of -23%. By adding a 7.5-sec delay on the rupture time to account for the delay in arrival of larger amplitude energy as observed in the raw accelerograms (Fig. 2), the VR increased to -2.9%. Increasing the dislocation rise time from 3 to 6 sec increased the VR to 43% and a dislocation rise time of 12 sec gave VR = 32%. All of these simplified inversions fail to adequately explain the data, although they do demonstrate that the data favors a dislocation rise time of approximately 6 sec. The F statistic for the best single time window run (dislocation rise time of 6 sec) with respect to the preferred model is 4.42. The improvement in fit over the critical F-value ($F = 1.04$) indicates that the multiple time window inversion provides a very significant improvement in fit.

Forward Tests of Finite Source Model

To examine the resolution of the preferred model we simulated seismograms using only portions of the total model (e.g., regions bounded by white lines in Fig. 3). Asperity A (Fig. 6) released a moment of 1.53×10^{27} dyne cm and contributed most to the synthetic waveforms at stations from the central part of the fault and to the south. For example, stations TCU071, 072, and 075 are modeled quite well using only the slip from asperity A. In comparison stations TCU039, 128, 068, and 052 are poorly modeled. Asperity B has a scalar moment of 1.3×10^{27} dyne cm and contributes most to stations near Shanyi (TCU068, 052, 128, 039, 029, 045). This asperity is shallow and is responsible for the large HPGV and static surface offsets. This asperity contributes to the later portions of seismograms located south of TCU052 and does not contribute at all to stations located south of the epicenter in the 50 sec that we model (cf. Fig. 7A, 7). Asperity C releases 7.6×10^{26} dyne cm and contributes most to stations near Chusan. Asperity D contributed only to the waveforms at HWA058. There is no clear pulse from the forward modeling of asperity E.

Inspecting the forward-modeled waveforms, we found that in-phase energy from asperities A and B enhanced the major northward pulse and resulted in the very high HPGV at TCU068. For the stations within latitudes 23.75 N to 24.05 N, asperity A contributed to the early part of the waveform, while asperity B contributed to the later part of the waveform. Stations near the SW corner of the fault plane required asperity C. Figure 8 shows the fit to the data for the model without asperities D and E (our preferred model). The contribution from all slip except asperities D and E results in a variance reduction of 85.1%, compared with 87.1% for the total slip model, showing that only 2% improvement in fit came from asperities D and E. Thus about 98% of the total variance reduction comes from slip in shallow asperities. The small waveform contribution from asperities D and E and their effect of elevating the scalar moment over the long-period estimates leads us to caution their interpretation.

Interpretation of the Preferred Model

In the previous section we found that with the available station coverage we can resolve the slip in asperities A–C of the preferred model (Fig. 3) and that slip in asperities D–E contributes little to the fit to the velocity waveforms. Additionally, we found that models that allow for variable rake and multiple time windows significantly improve the fit to the data. In this section, we examine these features in more detail and interpret the results.

The slip in each of the 10 time windows is shown in Figure 9. Asperity A had 1 m of slip that ruptured in the first two time windows. The slip then subsided until the sixth time window (9 sec later), when the major rupture occurred. Asperity B was found to be very complex and showed temporal rake rotation. It initiated at depth in the early time windows, and the rake rotates from mainly strike slip to dip slip. In the sixth time window the shallow patch started to rupture with initially pure reverse slip, which is seen to rotate to strike slip though the time windows 7–9. The total slip shown in Figure 3 is obtained by summing the contributions from each of the time windows. The total slip near the hypocenter is about 8 m. Near the northern end of the fault it reached 23 m, however, it is concentrated on a single subfault. Asperity C reached a peak of 3 m of slip.

The dislocation rise times at four locations (Fig. 3) are studied in detail (Fig. 10). Using a rupture velocity of 2.6 km/sec all of them showed an 8–10 sec delay except the one at the hypocenter. Location 1 near the maximum slip site of asperity B showed very high particle velocity (240 cm/sec) that is comparable to the maximum recorded HPGV of 390 cm/sec at station TCU068. At this site the dislocation started 28 sec after the origin time, and the dislocation rise time is about 8 sec. Location 2 is along the boundary between asperity A and asperity B. It shows a similar pattern to location 1 but with lower peak velocity (86 cm/sec) and 5-sec dislocation rise time. Location 3 within asperity A shows a peak particle velocity of 168 cm/sec and 10-sec delay. The dislocation rise time is about 5 sec. At the hypocenter (location 4) there were two pulses 5 sec apart with a peak particle velocity of 110 cm/sec. On average the particle velocity ranges from 70 to 250 cm/sec, and the stress drop ranges from 2 to 13 MPa for the primary asperities. Both quantities seem to increase northward. The different HPGA/HPGV ratios in the northern part of the fault compared to the south is probably related to the differences in moment rate. Figure 10 shows that the duration of the pulses in the southern half of the fault is shorter (approximately 2–8 sec, location 3) while on average they are longer in the northern half of fault (4–12 sec). The rupture process seems more complex in the

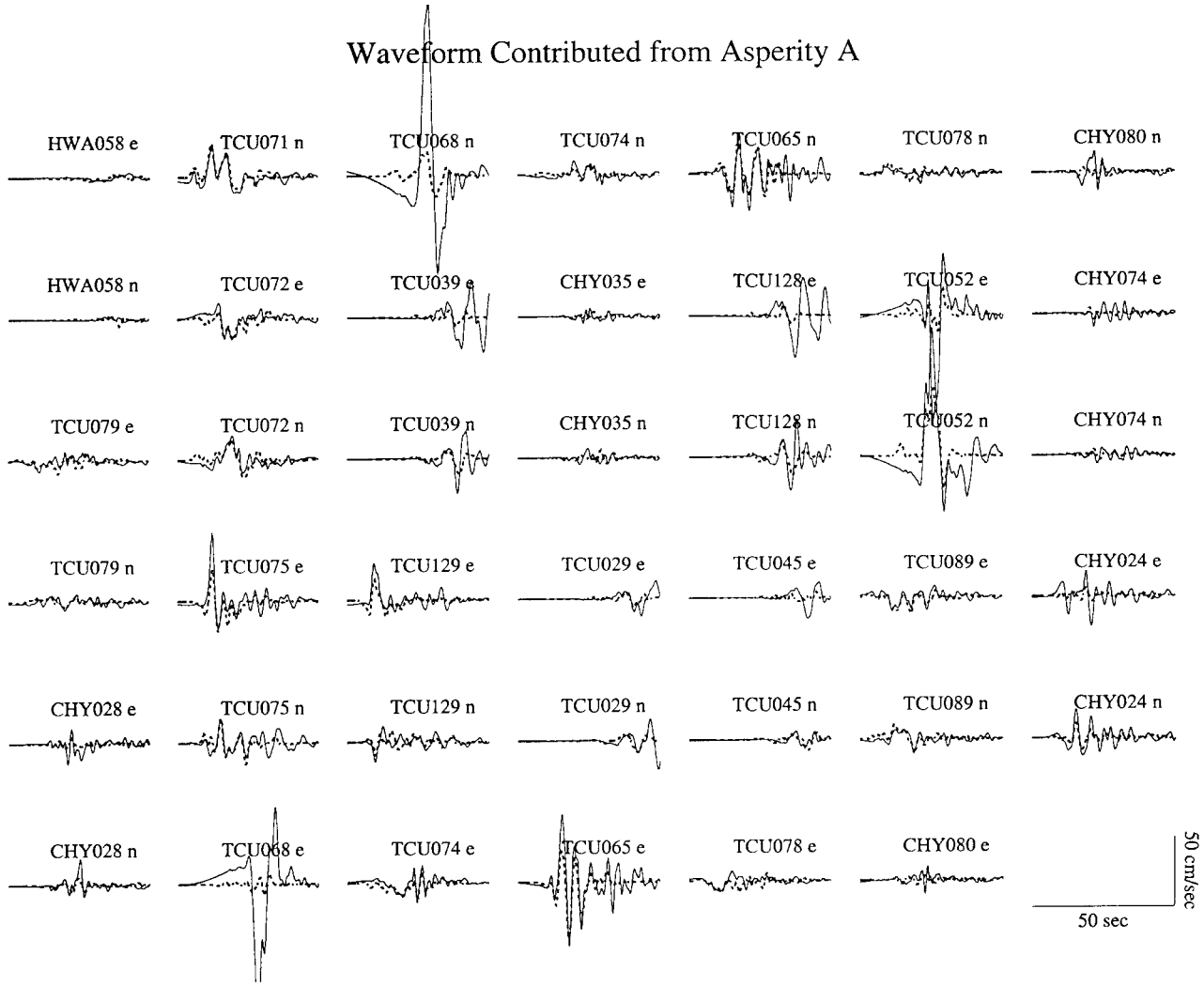

Figure 6. Synthetic velocity waveform (dashed lines) simulated using only asperity A. Solid traces are the recorded data. Most of the stations within the latitudes of 23.75 and 24.15 are mainly controlled by asperity A, especially TCU052 and 065. See Figure 1A for station locations.

south, where two source pulses are observed. The relatively short duration of the two pulses may contribute to proportionally more high-frequency radiation, thus leading to the large observed HPGA. In contrast, the northern end of the fault had only a single large pulse, which for some stations is partly due to constructive interference from both asperities A and B, producing the high HPGV in that region. The overall duration of the single pulse is longer, leading to a lower corner frequency and lower HPGA.

Next, we compare the moment rate function, spatial variation of the dislocation rise time, and perturbations to the rupture front (Fig. 11). The moment rate function is derived by integrating the moment distribution in the space domain, where this duration is the convolution of the dislocation rise time and rupture time integrated over the fault surface. There is a weak initiation, which is seen in the raw accelerograms (Fig. 2). After the first 5 sec, the moment rate is seen to increase steadily and peaks between 19 and 25 sec after the origin time. The moment rate function then decreases rapidly. The low levels of moment rate at times greater than 35 sec may not be well resolved. The total moment of 4.1×10^{27} dyne cm is about 53% of the moment derived from a teleseismic inversion study by Lee *et al.* (2000). However, it is larger than the 1.77×10^{27} dyne cm of Kao and Chen (2000), 2.4×10^{27} dyne cm of Yagi *et al.* (2000), and 2–4 $\times 10^{27}$ dyne cm of Ma *et al.* (2000). It is 21% larger than the Harvard CMT estimate (3.38×10^{27} dyne cm). We speculate that the larger moment comes from our use of higher frequency velocity seismograms, while Kao and Chen (2000), Ma *et al.* (2000), and Yagi (2000) use displacement seismograms. Another possibility is due to the 1D model we used for the Green's function calculation. Lack of low-velocity layers at shallow depths will reduce the amplitude of the Green's function, thus increasing the

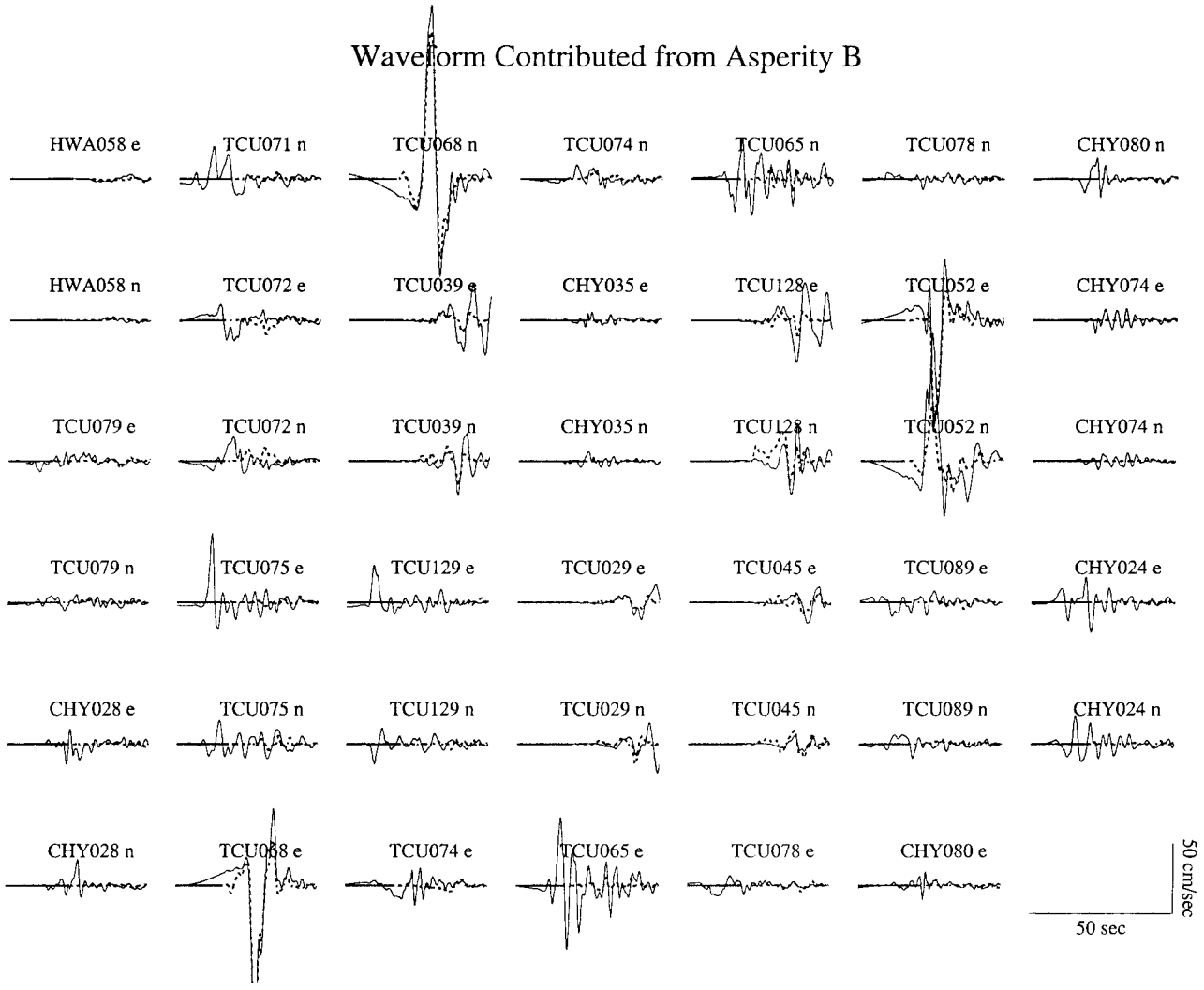

Figure 7. Synthetic velocity waveform (dashed lines) simulated using only asperity B. Solid traces show data. Note that this asperity contributed major portion of the waveform at TCU068 and TCU052. Because there is a large strike-slip component at shallow depth, the synthetics show a very strong northward directivity effect. The stations that are north of this asperity have larger amplitudes than to the south at similar distance (e.g., TCU128 N component vs. TCU065 N component). This asperity contributed to the later portion of the waveform for many stations (e.g., TCU079, TCU075, TCU071, TCU065). See Figure 1a for the station locations.

slip magnitude (e.g., Wald *et al.,* 1996). Complex 3D crustal velocity structure might also influence wave propagation paths, however, we believe our site selection process removed sites that either displayed or would be expected to have significant 3D influence.

We derived the rise time by counting the number of time windows that have continuous slip greater than 50 cm (Fig. 11b). The results for each subfault ranges between 6 and 10 sec, with little systematic variation. We have also plotted the wavefront time that includes the delay until slip in a single window exceeds 50 cm (Fig. 11c). This figure shows the rupture velocity was variable and overall slower than 2.6 km/sec. The rupture front slowed substantially as it propagated into the region between asperities A and B, suggesting a change in the dynamic properties of the rupture. Asperity B exhibits a temporal rake rotation (Fig. 9), which suggests that this part of the fault had a low initial stress and large stress drop (Guatteri and Spudich, 1998). Alternatively, it could be that the fault was strong and needed a dynamic perturbation to initiate the rupture. The rupture front is seen to delay as it reaches asperity B, suggesting that it has higher relative strength and a dynamic stress increase due to failure of other patches of fault needed to grow for asperity B to fail. (e.g., Ward, 2000). Apparently this change in the dynamics of the rupture process conspired to produce very large offsets and large particle velocities but relatively low

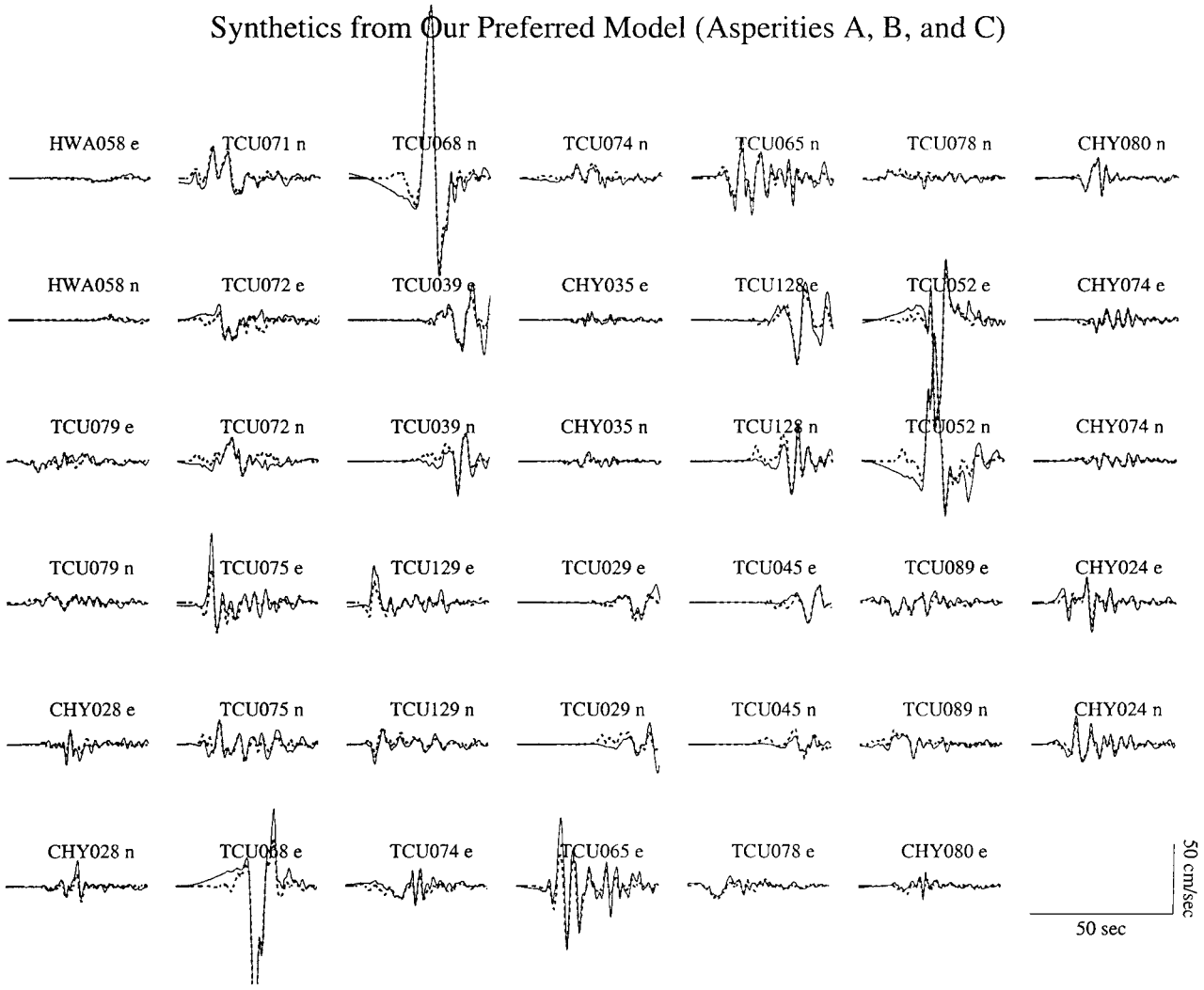

Figure 8. Synthetic waveforms (dashed lines) from the model without asperities D and E. The fit is very good, and the variance reduction between the synthetic and the observed data is 85%, compared with the variance reduction 87% obtained when the entire model is used. Thus 98% of the data is fit by waves radiated from asperities A–C. Asperities D and E are poorly resolved. Note the synthetics systematically underpredicted the first eastward pulse at stations located on the footwall near the surface rupture (TCU065, TCU075, TCU129).

radiation at high frequencies (Fig. 1). The interference of waves radiated from asperities A and B could also affect the spectrum and the HPGA and HPGV ratio.

Finally, the fault dimensions are important in the study of this earthquake because slip consistently occurred at the NE corner and the bottom of the fault plane model. To examine the resolution of the deep slip we extended the fault width by 25 more kilometers from the bottom and found that it resulted in unrealistically large slip (>25 m). As the previous sensitivity tests showed, this large slip can be introduced by just small variation of waveform, and therefore with the available strong-motion data, slip in asperities D–E is not well constrained. In fact, the addition of more stations to the east suppresses this slip without affecting the slip in asperities A–C. The northern bend of the surface rupture near asperity B could be related to the large slip along the Shanyi-Puli belt. Such unmodeled complexity could result in the rake rotation that we obtained. Investigation of nonplanar slip models will be the focus of future work.

Conclusion

We inverted the dense strong-motion data from the CWB to study the finite source process of 1999 Chi-Chi earthquake. More than 80 inversions using 41 velocity seismograms were performed, and our best model is comprised of three shallow asperities, which account for 98% of the total waveform fit. Deeper asperities are poorly constrained

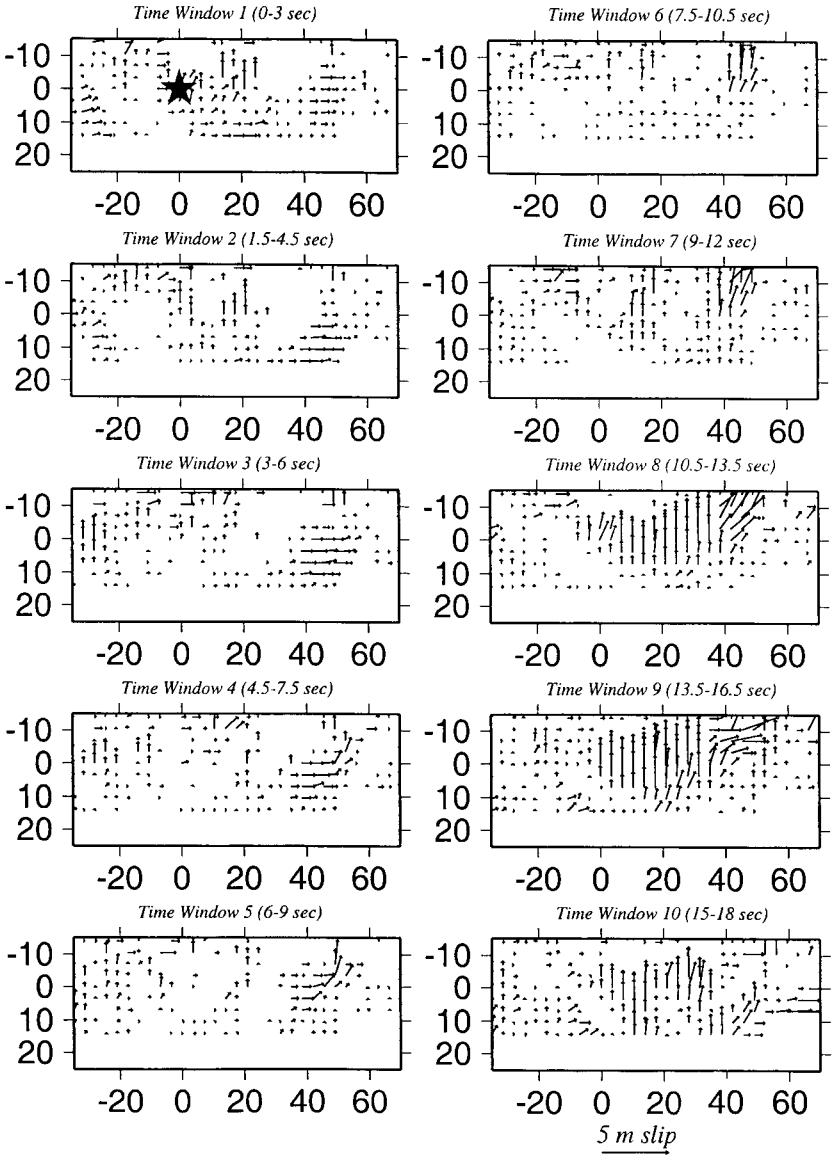

Figure 9. Slip vectors from the 10 time windows (without asperities D and E). Asperity A has mainly dip slip that started at the first two time windows. It then subsided for 7.5 sec before the second pulse started. Asperity B shows a rotation of rake from strike slip to dip slip to strike slip, which might be related to a dynamic stress change during the rupture process and low initial stress (Guatteri and Spudich, 1998). Asperity C shows mainly oblique slip.

and are likely artifacts. Asperity A, mainly dip slip, extends from the hypocenter to the northern end of the surface rupture. There are two pulses in this asperity separated by 5 sec, each with a duration if 3–4 sec. The particle velocity reaches 80 cm/sec. Asperity B, which is mainly left-lateral oblique slip, is confined within the region from the town of Puli to the northern end of the surface rupture. It is dominated by a large pulse with a dislocation rise time of 7 sec resulting in a particle velocity of 240 cm/sec. The high HPGA near the epicenter may be due to the multiple short duration rupture pulses in that region. The high HPGV at the northern end of the surface rupture is related to the single long duration pulse, which in part results from the constructive interference of waves from both asperities A and B. The rotation of rake of asperity B suggests that this region of the fault had relatively low initial stress and large stress drop. However it may also be due to the assumption of a single planar fault geometry, although surface slip measurements (CGS, 2000) and GPS (Yu *et al.,* 2001) indicate that oblique slip is required in this region of the fault. The observed northward directivity is mainly due to asperity B due to its significant strike-slip component. Asperity C is located south of the epicenter and is comprised of many smaller patches of slip. The total moment from those three asperities is 4.1×10^{27} dyne cm, released over a period of 30–35 sec. A range of rupture velocity between 2.0 and 2.9 km/sec provided good fit, with the best being 2.6 km/sec. The multiple time window analysis revealed that the rupture front slowed as it entered asperity B suggesting that it had low initial stress and required dynamic stress increases due to adjacent slipping patches of fault before failing (e.g., Ward, 2000), or that the actual rupture occurred on a surface different from

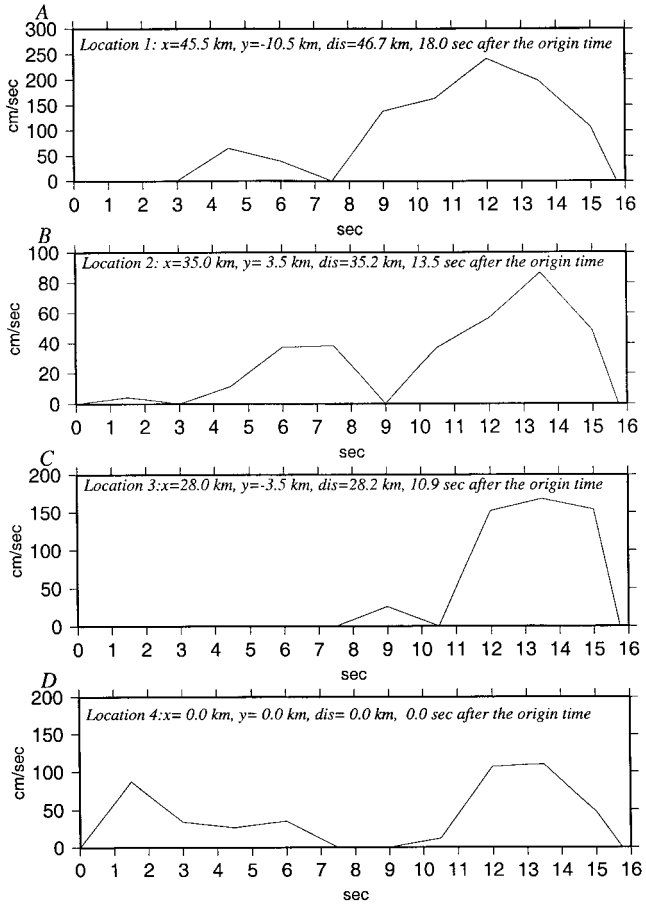

Figure 10. Dislocation rise-time functions from the four fault locations labeled on Figure 3. Most of the subfaults showed a delay of about 9 sec before the main rupture occurred, with the exception of the hypocenter, where there are two pulses (D). The particle velocity varies at different locations. Overall, asperity A has a lower particle velocity (<1.2 m/sec), while asperity B has a higher particle velocity (>2 m/sec).

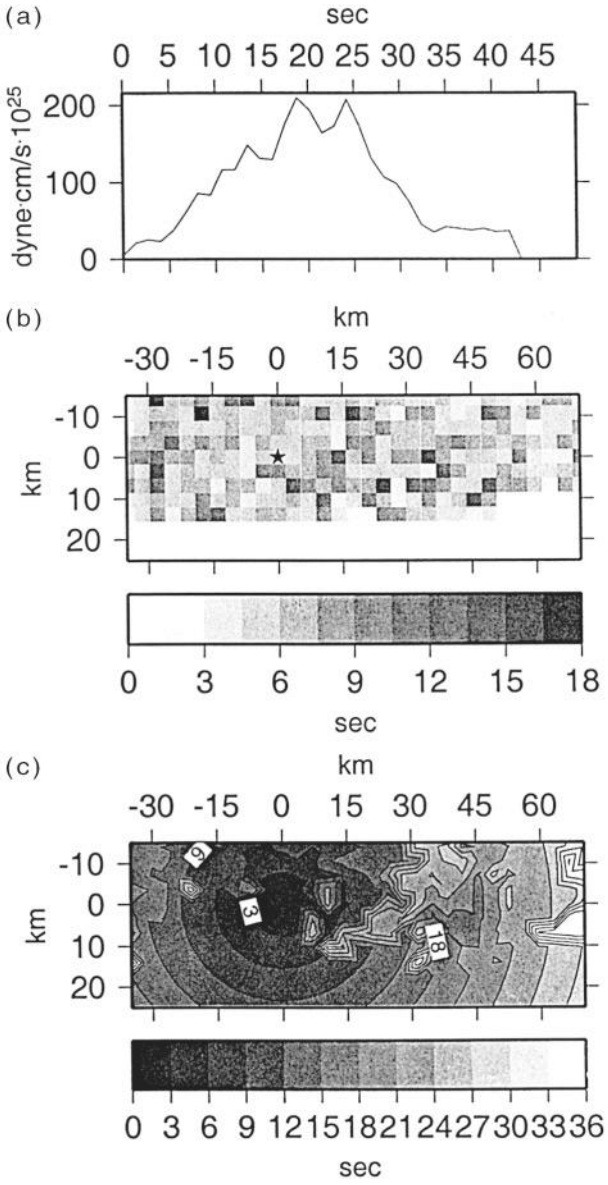

Figure 11. (a). Average moment rate function showing that the major moment was released over a period of 30 sec and peaked between 19 and 25 sec after the origin time. The rupture duration for each subfault (b) was calculated as the time span in which a subfault has continuous slip greater than 50 cm. The rupture time (c) calculated from the first time window that has greater than 50 cm slip. The delay for that particular time window from the origin time was added to the time it took for the waveform front to reach the subfault with a velocity of 2.6 km/sec. This showed a retardation of rupture when the rupture reached asperity B and the belt between Puli and Chusan. The rupture front is also seen to slow at shallow depth.

the modeled planar fault. The slip distribution that we obtain is mainly confined within a triangular area bounded by the towns Shanyi, Puli, and Chusan that seems to correlate with topography and pre-event seismicity and may be an expression of fault segmentation.

Acknowledgments

We thank the Central Weather Bureau for maintaining the strong-motion network that made this study possible. We also thank Dr. Willie Lee and Professor Leon Teng for facilitating the prompt release of strong-motion data. We are grateful to the Central Geological Survey for providing the surface rupture information. We thank David Schmidt for his review of this article and constructive criticism. This research is partially funded by the Soong's Foundation fellowship and NSF Grant EAR-0105998. The author (WCC) wishes to thank Professors Dietrich and Kirchner for supporting his trip to Taiwan to investigate the surface faulting from their NSF Grant EAR-0000893. This is Contribution Number 01-04 of the UC Berkeley Seismological laboratory.

References

Central Geological Survey (1999). Special Report on Chi-Chi 921 Earthquake, Central Geological Survey of Taiwan, December 1999, 315 pp. (in Chinese).

Chang, G., Y. M. Wu, and T. C. Shin (2000). Relocating the 1999 Chi-Chi Earthquake, Taiwan, *TAO* **11,** 581–590.

Cheng, W. B. (2000) Three-dimensional crustal structure around the source area of the 1999 Chi-Chi earthquake in Taiwan and its relation to the aftershock locations, *TAO* **11,** 643–660.

Chi, W.-C., D. Dreger, W. Cheng, and S. Larsen (2000) Preliminary study of 3D structural effects on the ground shaking of the Taiwan Chi Chi earthquake, *EOS Trans. Am. Geophys. Union* **81,** WP107.

Chiu, H., and H. Huang (2000) Strong ground motions and earthquake damages observed from the Chi-Chi Earthquake, *EOS Trans. Am. Geophys. Union* **81,** WP145.

Dreger, D., and A. Kaverina (2000) Seismic remote sensing for the earthquake source process and near-source strong shaking: a case Study of the October 16, 1999 Hector Mine Earthquake, *Geophys. Res. Lett.* **27,** 13,1941–13,1944.

Guatteri, M., and P. Spudich (1998) Coseismic temporal changes of slip direction: the effect of absolute stress on dynamic rupture, *Bull. Seism. Soc. Am.* **88,** 777–789.

Hartzell, S. H., and T. H. Heaton (1983) Inversion of strong ground motion and teleseismic waveform data for the fault rupture history of the 1979 Imperial Valley, California, Earthquake, *Bull. Seism. Soc. Am.* **73,** 1553–1583.

Kao, H., and W.-P. Chen (2000) The Chi-Chi earthquake sequence: active, out-of-sequence thrust faulting in Taiwan, *Science* **288,** 346–349.

Kaverina, A., D. Dreger, and E. Price (2000) Source Process of the October 16, 1999 Hector Mine Earthquake (Mw 7.2) from the inversion of the broadband regional data, *J. Geophy. Res.* (submitted).

Lee, S., K. Ma, J. Mori, and S. Yu (2000). Teleseismic and GPS data analysis of the 1999 Chi-Chi, Taiwan, Earthquake, *EOS Trans. Am. Geophys. Union* **81,** WP105.

Lee, W. H. K., T. C. Shin, K. W. Kuo, and K. C. Chen (1999). CWB free-field strong-motion data from the 921 Chi-Chi Earthquake, digital acceleration files on CD-ROM, prepublication version (December 6, 1999), Vol. 1, Seismology Center, Central Weather Bureau, Taipei, Taiwan.

Lin, C. (2000). Tectonic implication of both background seismicity and aftershocks of the 1999 Chi-Chi Earthquake, *EOS Trans. Am. Geophys. Union* **81,** WP107.

Ma, K., and J. Mori (2000). Rupture process of the 1999 Chi-Chi, Taiwan Earthquake from direct observations and joint inversion of strong motion, GPS and teleseismic data, *EOS Tran. Am. Geophys. Union* **81,** WP104.

Mori, J., and K.-F. Ma (2000). Slip velocity estimates of the 1999 Chi-Chi, Taiwan Earthquake: new observations of fault dynamics, *EOS Trans. Am. Geophys. Union* **81,** WP140.

Rau, R.-J., and F. Wu (1995). Tomographic imaging of lithospheric structures under Taiwan, *Earth Planetary Sci. Lett.* **133,** 517–532.

Rau, R.-J., and F. Wu (1998) Active tectonics of Taiwan Orogeny from focal mechanisms of small-to-moderate-sized earthquakes, TAO **9,** no. 4, 755–778.

Saikia, C. K. (1994). Modified frequency-wave-number algorithm for regional seismograms using Filon's quadrature-modeling of L(g) waves in eastern North America, *Geophys. J. Int.* **118,** 142–158.

Wald, D., T. H. Heaton, and K. W. Hudnut (1996) The slip history of the 1994 Northridge, California, Earthquake determined from strong-motion, teleseismic, GPS, and leveling data, *Bull. Seism. Soc. Am.* **86,** 49–70.

Ward, S. N. (2000) San Francisco Bay Area earthquake simulations: a step toward a standard physical earthquake model, *Bull. Seism. Soc. Am.* **90,** no. 2, 370–386.

Wu, F. T. and R.-J. Rau (1998) Seismotectonics and identification of potiontial seismic source zones in Taiwan, *TAO* **9,** no. 4, 739–754.

Wu, C., M. Takeo, and S. Ide (2000). Source process of the Chi-Chi Earthquake, *EOS Trans. Am. Geophys. Union* **81,** WP104.

Yagi, Y., and M. Kikuchi (1999) Preliminary results of rupture process for the September 21, 1999 Chi-Chi Earthquake, *http://wwweic.eri.u-tokyo.ac.jp/yuji/taiwan/taiwan.html* (last accessed May 2000).

Yagi, Y., and M. Kikuchi (2000). Source rupture process of the Chi-Chi, Taiwan, Earthquake of 1999, obtained by seismic wave and GPS data, *EOS Trans. Am. Geophys. Union* **81,** WP104.

Yu, S. B., L. C. Kuo, Y. J. Hsu, H. H. Su, C. C. Liu, C. S. Hou, J. F. Lee, T. C. Lai, C. C. Liu, C. L. Liu, T. F. Tseng, C. S. Tsai, and T. C. Shin (2001) Preseismic deformation and coseismic displacements associated with the 1999 Chi-Chi, Taiwan earthquake, *Bull. Seism. Soc. Am.* **91,** no. 5, 995–1012.

Seismological Laboratory
University of California at Berkeley
Berkeley, California 94720-4767

Manuscript received 21 November 2000.